ACS APPLIED MATERIALS & INTERFACES

Research Article

www.acsami.org

Photocurrent Enhancement for Ti-Doped Fe_2O_3 Thin Film Photoanodes by an In Situ Solid-State Reaction Method

Chunhui Miao, Tongfei Shi, Guoping Xu, Shulin Ji, and Changhui Ye*

Anhui Key Laboratory of Nanomaterials and Technology and Key Laboratory of Materials Physics, Institute of Solid State Physics, Chinese Academy of Sciences, Hefei 230031, People's Republic of China

Supporting Information

ABSTRACT: In this work, a higher concentration of Ti ions are incorporated into hydrothermally grown Ti-doped (2.2% by atomic ratio) micro-nanostructured hematite films by an in situ solid-state reaction method. The doping concentration is improved from 2.2% to 19.7% after the in situ solid-state reaction. X-ray absorption analysis indicates the substitution of Fe ions by Ti ions, without the generation of Fe^{2+} defects. Photoelectrochemical impedance spectroscopy reveals the dramatic improvement of the electrical conductivity of the hematite film after the in situ solid-state reaction. As a consequence, the photocurrent density increases 8-fold (from 0.15 mA/cm^2 to 1.2 mA/cm^2), and it further increases up to ~1.5 mA/cm^2 with the adsorption of Co ions. Our findings demonstrate that the in situ solid-state reaction is an effective method to increase the doping level of Ti ions in hematite films with the retention of the micro-nanostructure of the films and enhance the photocurrent.

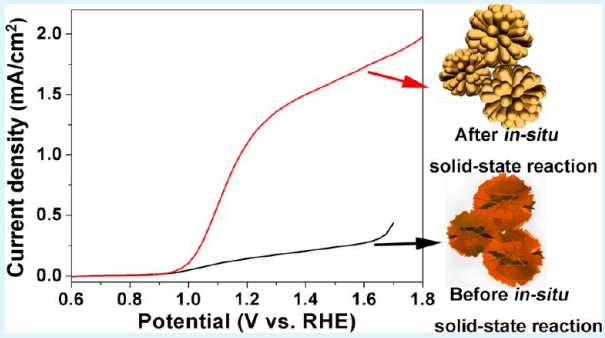

KEYWORDS: *in situ solid-state reaction method, Ti-doped hematite, photocurrent enhancement, Co ions adsorption*

INTRODUCTION

Recombination is a severe issue to be tackled before Fe_2O_3 can be widely adopted in photocurrent conversion, because of the short diffusion length of photogenerated holes.[1−4] To address this issue, recently, we have synthesized micro-nanostructured Ti-doped hematite films via a simple hydrothermal method.[1] Titanium doping has been demonstrated as an effective method to improve the conductivity of hematite,[1,5,6] where the enhanced electrical conductivity can extend the lifetime of the charge carriers, reduce the recombination of photogenerated electron−hole pairs, and lead to enhanced photocurrent. However, it is challenging to incorporate a sufficient amount of Ti ions in Fe_2O_3 via a hydrothermal method, because $TiCl_4$ in the mixed solution decreases the pH value and makes the precipitation of Fe^{3+} difficult.[7] We have shown that a maximum concentration of Ti ions of ca. 2.2 % (atomic ratio) could be incorporated in Fe_2O_3 via the hydrothermal method,[1] limiting the achievable photocurrent conversion efficiency.

It is well-known that solid-state reaction method is effective in introducing dopant ions into a material.[8−14] Introducing dopants into hematite via this method has been attempted by mixing powders mechanically, followed by thermal treatment.[8,9] However, the morphology of the starting Fe_2O_3 could not be preserved during the milling process. Here, we propose an in situ solid-state reaction method that could incorporate an amount of Ti ions as large as ca. 19.7% (atomic ratio) in Fe_2O_3, with the maintenance of the micro-nanostructure of the hematite films. The proposed method is illustrated in Scheme 1, where the original hematite films were synthesized by the hydrothermal method on fluorine-doped tin oxide (FTO)-coated glasses. $TiCl_4$ ethanol solution was directly dropped on the film, followed by annealing in the atmosphere to incorporate Ti ions. Compared to other methods, as listed in

Scheme 1. Diagram of the in Situ Solid-State Reaction Method: (a) Hematite Micro-nanostructure Synthesized via the Hydrothermal Method, (b) $TiCl_4$ Ethanol Solution Casting on Hematite Structures, (c) Hematite after In Situ Solid-State Reaction, and (d) Enlarged View of Panel (c)

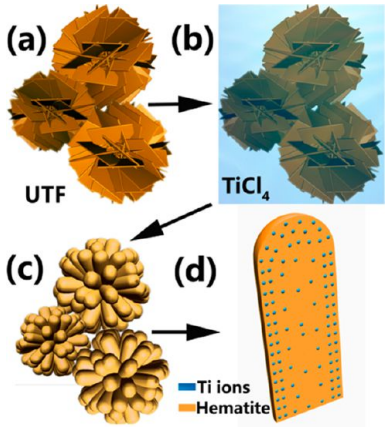

Received: November 5, 2012
Accepted: January 24, 2013
Published: January 24, 2013

Table 1, the as-proposed in situ solid-state reaction method in this work has the main advantages of being facile and cost

Table 1. Brief Overview of Doped Hematite Films Reported in the Literature[a]

ref	method	dopant	concentration (%)	photocurrent density (mA/cm^2)
13	hydrothermal followed by spin-coating and annealing	Cr	ca 1.4	~0.05
15	molecular beam epitaxy	Ti	15	
16	spin-coating	Ti	7.75	~0.1
17	radio frequency magnetron sputtering	Ti	1.8	~0.02
18	atmospheric pressure chemical vapor deposition	Si	1.5	2.2
our work	hydrothermal method	Ti	2.2	0.15
our work	in situ solid-state reaction	Ti	19.7	1.2

[a]Photocurrent measurements were recorded at 1.23 V vs RHE with 1 M NaOH electrolyte under 1 sun AM 1.5G condition.

effective, with the photocurrent density being comparable or better.

Further improved photocurrent conversion performance could be achieved by engineering the interface between the hematite and the electrolyte,[1,19−22] such as the adsorption of Co ions to reduce surface recombination,[18,22−25] although the role of Co ions as electrocatalyst or interface passivation is still under debate. In this work, we employed photoelectrochemical impedance spectroscopy (PEIS) method to elucidate the exact role of the Co ions in enhancing the photocurrent conversion performance. Compared to transient absorption spectra (TAS),[19,23] the analysis result of PEIS is more straightforward.

EXPERIMENTAL SECTION

Synthesis of Ti-Doped Hematite Photoanodes by the In Situ Solid-State Reaction Method. As reported in previous work,[1] we synthesized Ti-doped (2.2%) micro-nanostructured hematite by the hydrothermal method. In this work, to increase the doping concentration of Ti ions in hematite films, we proposed an in situ solid-state reaction method. Briefly, a 10 μL $TiCl_4$ ethanol solution was dropped onto the as-synthesized α-Fe_2O_3 films (Ti-doped, 2.2%) followed by annealing at 650 °C for 10 h. After heat treatment, the samples were cleaned by rising with deionized water for several times and dried by a stream of dry nitrogen. The notations for the respective samples (concentration of $TiCl_4$ dropped) were UTF (untreated sample prepared by hydrothermal method with 2.2% doping concentration), STF-1 (0.25%), STF-2 (0.5%), STF-3 (1%), STF-4 (2%), and STF-5 (5%), respectively.

Adsorption of Co Ions on Hematite Films. The Co ions were adsorbed on the surface of hematite films by dipping the electrodes into a 50 mM $Co(NO_3)_2$ solution for 20 s, followed by rinsing with deionized water and drying in nitrogen.

Characterizations. The characterizations were conducted at room temperature. The crystalline phase of the samples was identified by X-ray diffraction (XRD) using a Philips X'Pert Pro MPD with Cu Kα (λ = 1.5406 Å) radiation. The morphology of the samples was determined by field-emission scanning electron microscopy (FESEM) (FEI, Model Sirion-200) coupled with energy-dispersive X-ray analysis (EDX). Optical absorption measurements were performed using a UV-visible absorption spectrometer (Shimadzu, Model UV 3600). X-ray photoelectron spectra (XPS) were recorded using an electron spectrometer fitted with an Al Kα source (Thermo ESCALAB, Model 250, soft X-ray source at 1486.6 eV). *K*-edge X-ray absorption near-edge spectra (XANES) and extended X-ray absorption fine-structure (EXAFS) were measured on beamline BL14W1 at Shanghai Synchrotron Radiation Facility (SSRF).

PEIS and photocurrent measurements were conducted using an electrochemical workstation (Zahner IM6ex) in a three-electrode electrochemical system with 1 M NaOH electrolyte under 1 sun AM 1.5G condition, using a 3A Class solar simulator (back-side illumination). Cyclic voltammetry (CV) was measured in darkness. Platinum foil was used as the counter electrode. The measured potentials vs Ag/AgCl (sat. KCl) reference electrode were converted to the reversible hydrogen electrode (RHE) scale, according to the following Nernst equation:

$$E_{RHE} = E_{Ag/AgCl} + 0.059pH + E^{\circ}_{Ag/AgCl}$$

where E_{RHE} is the converted potential vs RHE, $E^{\circ}_{Ag/AgCl}$ = 0.1976 V at 25 °C, and $E_{Ag/AgCl}$ is the experimentally measured potential against the Ag/AgCl (sat. KCl) reference electrode.

RESULTS AND DISCUSSION

Morphology, Phase, Structure, and Absorbance Characterizations. The UTF film was confirmed to be α-Fe_2O_3 by XRD analysis, as shown in Figure 1. The intense

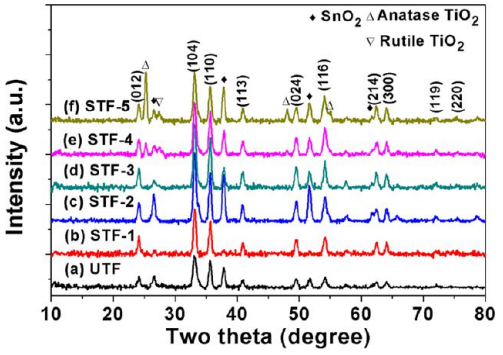

Figure 1. XRD patterns of α-Fe_2O_3 films: (a) UTF, (b) STF-1, (c) STF-2, (d) STF-3, (e) STF-4, and (f) STF-5.

peaks of the XRD pattern indicate that the α-Fe_2O_3 product was well-crystallized. The crystal structure of the films after the solid-state reaction (STF samples) was also determined by XRD. For STF-1 and STF-2, no other crystalline phase except SnO_2 was present. Continually increasing the concentration of $TiCl_4$ dropped on the hematite films led to the formation of a mixture of anatase and rutile TiO_2 on the surface of the films.

The morphologies of the hematite films were revealed by SEM observations. From the SEM images, the morphologies of the samples after the in situ solid-state reaction remained the pinenut-like ball micro-nanostructures although the fine nanoscale structure changed slightly (Figure 2).

XPS analysis was performed to confirm the incorporation of Ti ions into hematite films. XPS data showed that the concentration of Ti ions in STF hematite films increased with the concentration of $TiCl_4$, in consistence with the XRD results. EDX analysis showed the same trend (Figure S1 in the Supporting Information); however, the calculated atomic ratios were smaller than the corresponding XPS results (Table S1 in the Supporting Information), which is reasonable, because XPS could only detect the surface of the samples,[26−28] where the concentration of Ti ions might be higher than in the interior. The trend of the doping ratio is consistent with the

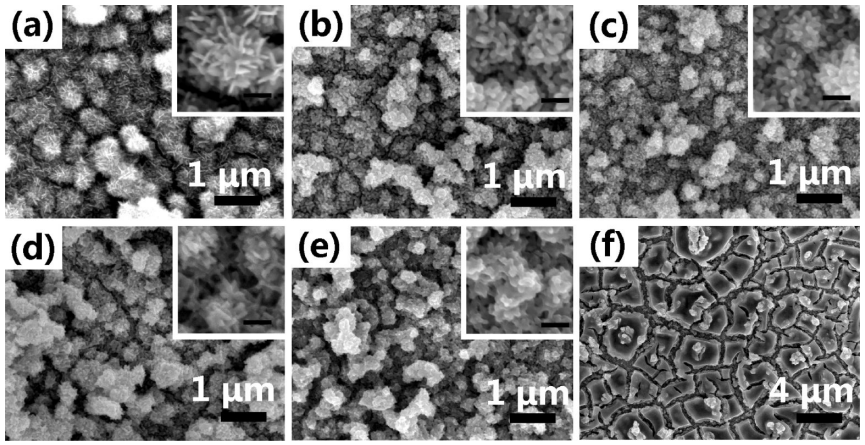

Figure 2. SEM images of α-Fe_2O_3 films: (a) UTF, (b) STF-1, (c) STF-2, (d) STF-3, (e) STF-4, and (f) STF-5. The insets are the enlarged images of the corresponding samples. The scale bar in the insets is equal to 200 nm.

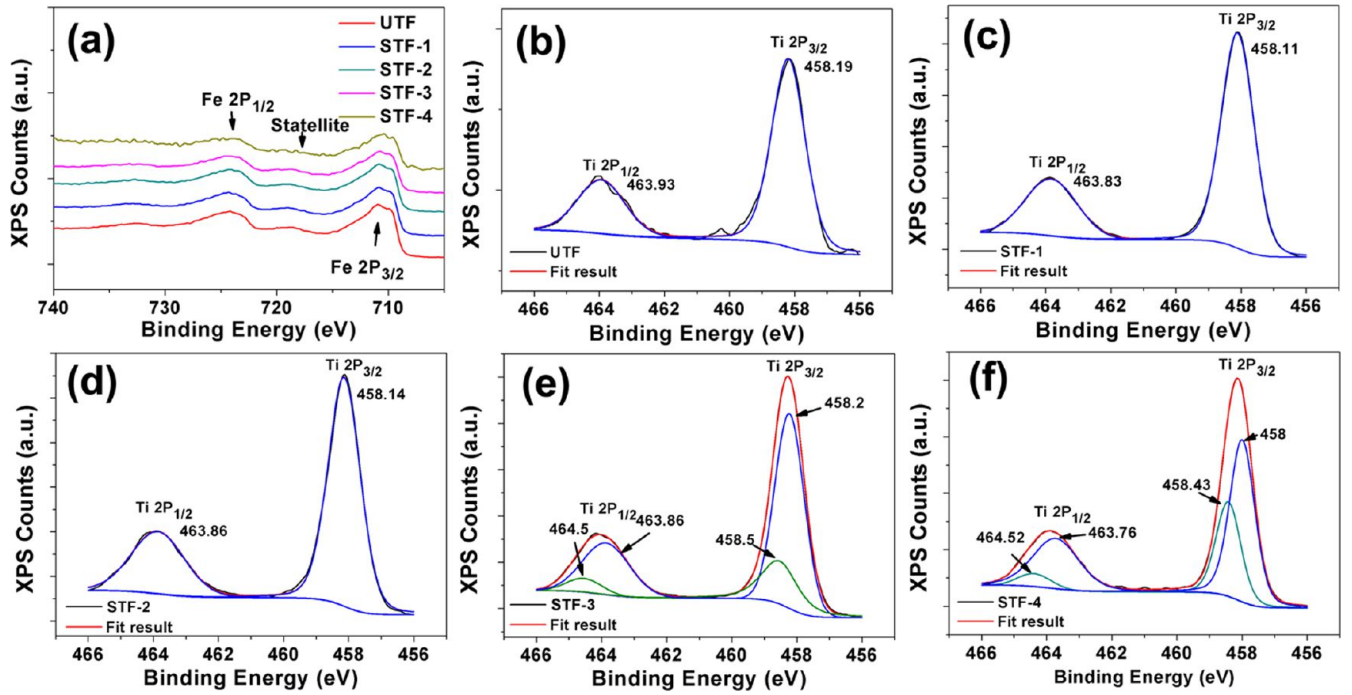

Figure 3. X-ray photoelectron spectroscopy (XPS) spectra of (a) Fe 2p, Ti 2p recorded from (b) UTF, (c) STF-1, (d) STF-2, (e) STF-3, and (f) STF-4.

conductivity and the photocurrent measurements, as shown in the subsequent sections.

XPS performed on the samples revealed that Ti was in the +4 state. For UTF, STF-1, and STF-2, the $2p_{3/2}$ peak is ~458.15 eV, agreeing well with the 2p binding energy of Ti^{4+} ions.[29−31] However, compared to the reported value for TiO_2 (458.5 eV for $2p_{3/2}$ binding energy),[29,32] a red shift of ~0.4 eV occurs, indicating the different microenvironment of Ti^{4+} ions in α-Fe_2O_3 from that in pure TiO_2. By curve fitting of the Ti $2p_{3/2}$ for STF-3 and STF-4 multiplet peaks, we obtained binding energies of ~458.15 eV and ~458.5 eV, respectively, with the former being the same to that of STF-1 and STF-2, and the latter the same to pure TiO_2, further confirming the excessive TiO_2 on the surface of the hematite films when the concentration of $TiCl_4$ was too large. We did not observe the presence of Fe^{2+} on the surface of the films from XPS characterizations (Figure 3a).[29,33,34]

The XANES technique offers a detailed picture of the local structure around Fe or Ti atoms. Figure 4a shows the Fe K-edge XANES for pure hematite and STF films. By comparing the fine detail of XANES curves of the STF films to that of pure α-Fe_2O_3 sample, we found that the local structure of Fe ions did not change due to the introduction of Ti ions, indicating that most of the Fe ions are in the +3 charge state.

Figure 4b shows the Ti K-edge XANES spectra for STF-2, STF-3, and STF-4 samples. XANES spectrum for STF-2 shows the appearance of an obvious peak (labeled as A) in the pre-edge region and two main peaks (C and E), and another two small peaks around peak C were labeled as B and D, respectively. Assuming that Ti is substitutional, the calculated K-edge XANES (using Feff 8.4 code)[35] was also shown in Figure 4b, where the curve shape closely resembles that of the Ti K-edge of STF-2, indicating that the vast majority of Ti atoms in this sample occupy cationic lattice sites. Comparing

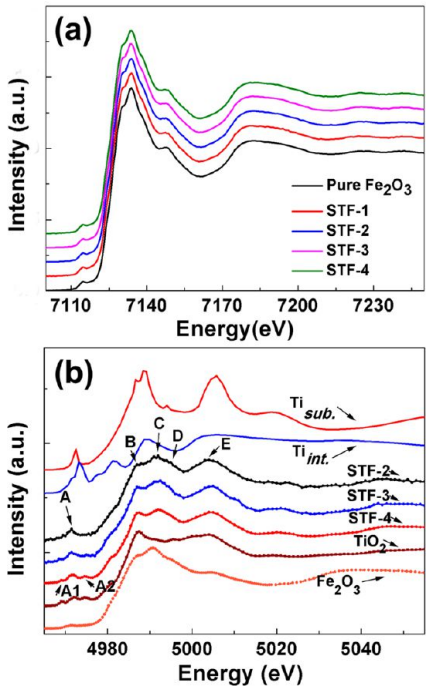

Figure 4. (a) Fe K-edge XANES spectra for pure α-Fe_2O_3 and STF samples; (b) Ti K-edge XANES spectra for the STF samples as well as TiO_2 and pure α-Fe_2O_3. The calculated K-edge XANES curves assuming Ti ions on the substitutional site (Ti_{sub}) or Ti ions on the octahedral interstitial site (Ti_{int}) are also shown.

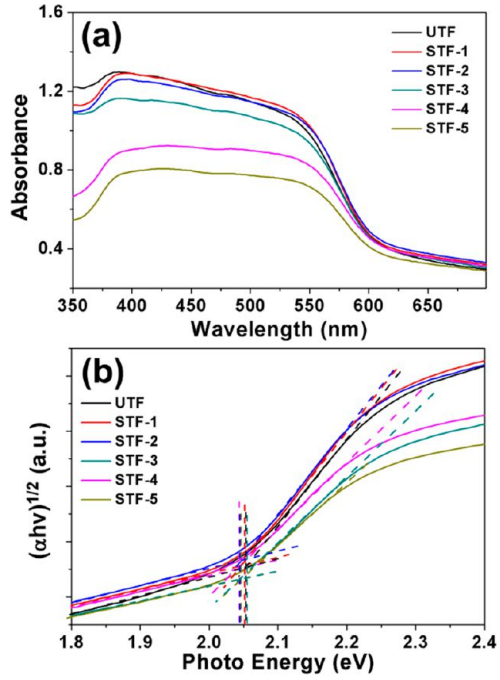

Figure 5. (a) UV-vis absorption spectra and (b) Tauc plots for UTF and STF samples.

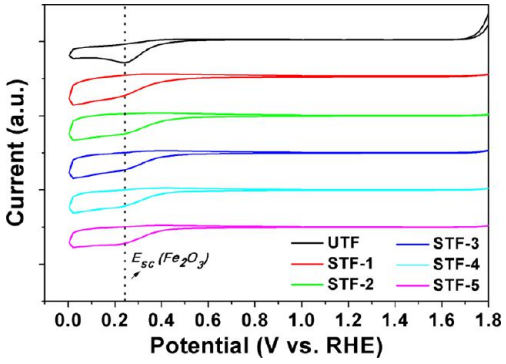

Figure 6. Cyclic voltammograms recorded on UTF and STF samples.

the shape of the STF-2 curve to that of the Fe K-edge from the pure hematite film, we found that the two curves are similar in shape, again confirming that Ti atoms occupy cationic lattice sites, because the line shape is dependent primarily on the structure surrounding the absorbing atom.[15,36] Moreover, there is no evidence for interstitial Ti (Ti_{int}), because the shape of the STF-2 curve differs from that of the calculated Ti_{int}. Such a result was consistent with the result reported by Magnan et al.[37] Moreover, the intensity of peak B increases with the concentration of $TiCl_4$, and peak A splits into three peaks (A1, A, and A2). Comparison with the Ti K-edge XANES spectra of TiO_2 proves the presence of TiO_2 in both STF-3 and STF-4.

Positions of the Conduction and the Valence Band. Figure 5 shows the light absorption spectra of UTF and STF films. The spectra display features typical of α-Fe_2O_3 films with an absorption onset of ~595 nm. The band-gap values were determined from the Tauc plots (Figure 5b) and were found to be approximately the same for all the samples, exhibiting an indirect transition at ~2.05 eV.

Figure 6 shows the CV curves, where cathodic peaks corresponding to the conduction band position (more appropriately, the shallow donor level) of α-Fe_2O_3 electrodes could be observed.[1,38,39] The valence band position could be determined combined with the band-gap value obtained from optical absorption analysis. Our results showed that the surface conduction band (E_{sc}) and valence band (E_{sv}) positions of α-Fe_2O_3 did not shift dramatically due to Ti-dopant introduction, in agreement with our previous observation.[1]

Photocurrent, Mott–Schottky Plots, and Photoelectrochemical Impedance Spectroscopy. The photocurrent conversion of the STF films was investigated as a function of the concentration of $TiCl_4$. Figure 7a compares the linear sweep of UTF, annealed UTF (UTF annealed at 650 °C for 10 h in the atmosphere without $TiCl_4$ dropped), and STF films. The photocurrent densities of the STF films are much larger than that of both UTF and annealed UTF. The photocurrent density increases as the doping concentration increases and reaches a maximal value when the concentration of $TiCl_4$ is 0.5% (STF-2). Further increasing the concentration of $TiCl_4$ leads to the decrease of the photocurrent, because the surface roughness factor decreases. Because of the excessive TiO_2 on the surface of the films, the photocurrent onset potential of STF-3, STF-4, and STF-5 shifted to the negative direction, compared to UTF, STF-1, and STF-2, since the valence band position of TiO_2 is negative than that of Fe_2O_3. Instead of using a higher concentration of $TiCl_4$, we repeated the treatment of the films with 0.25% $TiCl_4$. As shown in Figure S2 in the Supporting Information, the maximal photocurrent was obtained by treating UTF, and further treatment led similarly to the decrease in photocurrent density.

We have also investigated the effect of annealing on photocurrent conversion. The photocurrent density of the annealed UTF was improved compared to UTF, which is due

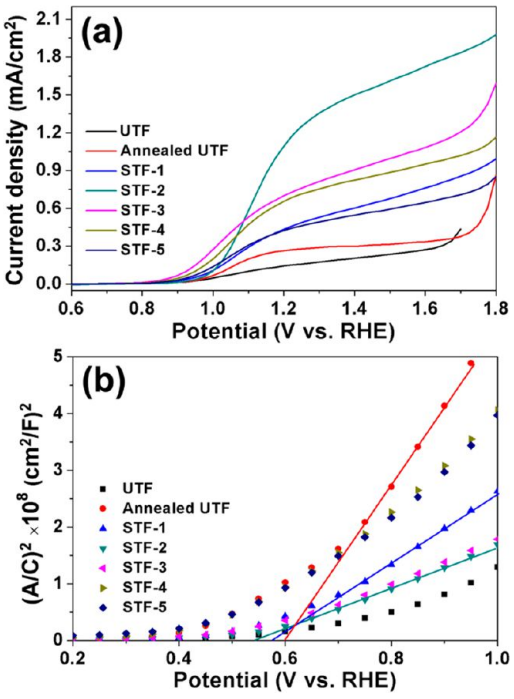

Figure 7. (a) *J*–*V* and (b) Mott–Schottky (M-S) plots of UTF, annealed UTF, and STF samples after in situ solid-state reaction.

to the improvement in the crystallinity and decrease of the defect density, as will be discussed in the following section. This observation is also true for hematite nanoarray films (see Figures S3 and S4 in the Supporting Information, the nanoarray film was prepared in the same way as UTF via a hydrothermal method, but without ethanol and $TiCl_4$). Annealing is also critical for the doping process. Because Ti ions could not be incorporated completely into hematite at lower temperatures, as shown in Figure S5 in the Supporting Information, the photocurrent density increases with the annealing temperature; however, higher temperature leads to the increase of the resistivity of the FTO glass. As shown in Table S2 in the Supporting Information, the optimum annealing temperature is ~650 °C. It is noteworthy that the in-situ solid-state reaction method also works well for nanoarray films. Figure S3 in the Supporting Information shows that the photocurrent density of a hematite nanoarray film increases dramatically after the $TiCl_4$ treatment (processing conditions were the same as those for STF-2).

Mott–Schottky (M-S) plots were employed to study the electric properties of UTF and STF samples. The films were analyzed in darkness in 1 M NaOH. M-S plots for the samples were recorded at 1000 Hz. As shown in Figure 7b, the slope of M-S plots of annealed UTF increases due to the decreased surface roughness and oxygen vacancy,[40−42] and a similar trend could be observed for a hematite nanoarray film, as shown in Figure S3 in the Supporting Information. The slope in the quasi-linear region of the M-S plots close to the flat-band potential (E_{fb}) was used to calculate the donor concentration of the films. The carrier density of annealed UTF, STF-1, and STF-2 is 2.89×10^{18}, 6.86×10^{18}, and 1.13×10^{19} cm^{-3}, respectively (see Table S3 in the Supporting Information). The flat-band potential shifted toward the negative direction with the doping concentration, which is a consequence of the modified doping concentration and the related upward shift of the Fermi level caused by titanium doping. Our experimental results indicate that the doping level increases with the concentration of $TiCl_4$. The enhanced electrical conductivity can extend the lifetime of the charge carriers, reduce the recombination of the electron–hole pairs, and lead to improved photocurrent.

Carrier densities of STF-3, STF-4, and STF-5 are difficult to determine, because of the uncertainty in measuring the surface roughness factors. Anyway, the diminished surface roughness factor led to the increased slope of M-S plots, and the higher conduction band position of TiO_2 made the flatband position of these electrodes shift in a negative direction.

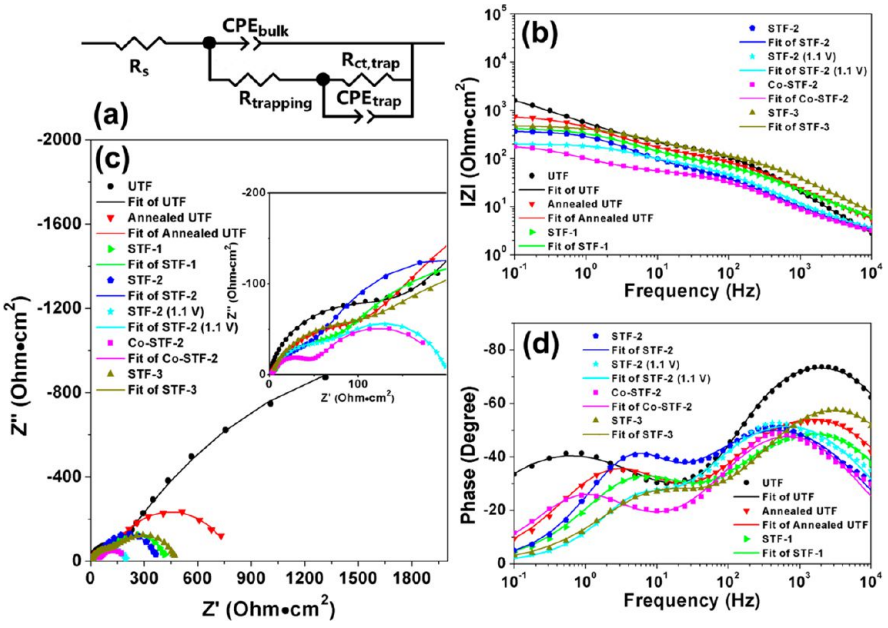

Figure 8. (a) Equivalent circuit, (c) Nyquist plots, and (b, d) Bode plots of UTF, annealed UTF, STF films, and Co ions adsorbed STF-2, measured at 1.05 V vs RHE (PEIS of STF-2 measured at 1.1 V was denoted) under 1 sun illumination.

PEIS analysis was adopted to further understand the role of the annealing process, titanium dopants, and the excessive TiO_2 in the photocurrent conversion processes. The electrical analogue that we used to fit the PEIS data is shown in Figure 8a. The resistance accounting for surface-state trapping electrons from the conduction band and holes from the valence band, acting as a recombination center, is given by $R_{trapping}$. Surface states affect the charge transfer of holes to the donor species in solution, which could be described as a resistance $R_{ct,trap}$. The trap-state capacitance was denoted as C_{trap}, and the space-charge capacitance (C_{sc}) and the series connection of C_h have been lumped into C_{bulk}. Finally, R_S is the series resistance of the cell.[43] Nyquist plots and Bode plots for UTF, annealed UTF, STF-1, STF-2, and STF-3 electrodes measured at 1.05 V vs RHE under 1 sun illumination are shown in Figure 8, and the equivalent circuit parameters obtained from fitting EIS data are summarized in Table 2. Compared to UTF,

Table 2. Equivalent Circuit Parameters Obtained from Fitting PEIS Data

sample	R_S (Ω)	C_{bulk} (F)	$R_{trapping}$ (Ω)	$R_{ct,trap}$ (Ω)	C_{trap} (F)
UTF	0.86	5.44×10^{-6}	150	3683	1.48×10^{-4}
annealed UTF	2.29	2.86×10^{-6}	143.2	652.5	1.50×10^{-4}
STF-1	2.74	3.03×10^{-6}	107.2	320.3	1.60×10^{-4}
STF-2	2.20	9.67×10^{-6}	105.6	270.4	2.06×10^{-4}
STF-2 (1.1 V)	2.10	7.55×10^{-6}	105	91.01	4.35×10^{-4}
Co-STF-2	2.23	1.20×10^{-5}	56.21	137.9	1.64×10^{-3}
STF-3	2.34	1.71×10^{-6}	135.1	349.7	6.70×10^{-5}

R_s of annealed UTF increased with the resistivity of the FTO glass and C_{bulk} decreased, in coincidence with the M-S plot results shown in Figure 7b. C_{trap} and $R_{trapping}$ remained the same, whereas $R_{ct,trap}$ decreased, indicating that photogenerated holes could be transferred from hematite to the electrolyte more efficiently. Such a result well explains the higher photocurrent density after the annealing process. Compared to annealed UTF, the $R_{ct,trap}$ and $R_{trapping}$ values of the STF samples are reduced and the C_{trap} value is increased as the concentration of $TiCl_4$ is increased. Increased C_{trap} means that more holes could be stored in the intermediate states, facilitating the participation of the holes in the photocurrent conversion processes. The decrease of $R_{ct,trap}$ and $R_{trapping}$ indicates that Ti ions introduced by in situ solid-state reaction could facilitate charge transfer of holes to the donor species in solution, suppress the recombination of photogenerated electron–hole pairs, and improve the photocurrent.

By further increasing the amount of $TiCl_4$, the $R_{ct,trap}$ and $R_{trapping}$ values increased and the C_{trap} value decreased, implying that excessive TiO_2 led to the increase of the surface recombination and the decrease of the photocurrent density, compared to that of STF-2.

Adsorption of Co Ions. Figure 9a shows the linear sweeps of STF-2 and Co-adsorbed STF-2 (Co-STF-2) photoanodes measured under 1 sun illumination. The adsorption of Co ions produced a 100-mV cathodic shift of the photocurrent onset potential and increased the photocurrent density from 1.2 mA/cm^2 to 1.38 mA/cm^2 (at 1.23 V vs. RHE). M-S plots before and after Co-ion treatment are shown in Figure 9b, where the overlap of the plots means that neither the carrier density nor

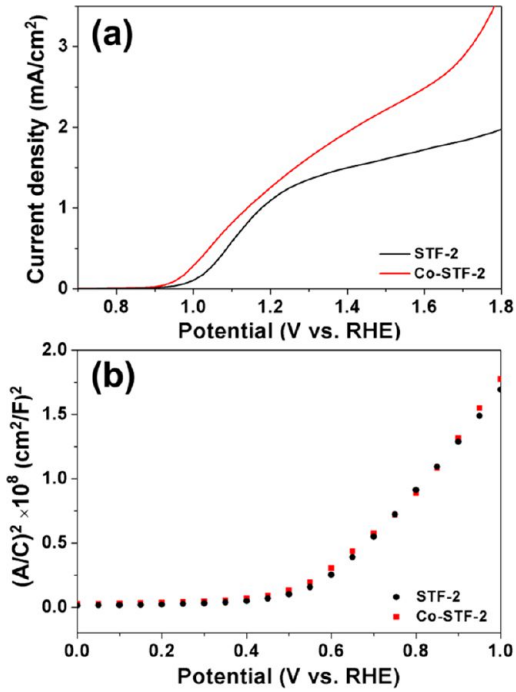

Figure 9. (a) $J-V$ characteristics and (b) M-S plots of STF-2 and Co-STF-2 electrodes.

the flatband potential changed much due to the adsorption of Co ions.

PEIS analysis was performed to understand the role of Co ions played in photocurrent conversion processes. The most striking effect of the adsorbed Co ions upon the PEIS data is a dramatic decrease of $R_{ct,trap}$ and $R_{trapping}$. Another significant impact is the increase of C_{trap}, which means photogenerated holes could be stored in surface states and could be transferred to electrolyte more easily. Fitting the PEIS data of STF-2 collected at 1.1 V (vs RHE) shows that C_{trap}, $R_{ct,trap}$, and $R_{trapping}$ changed in the same direction with the adsorption of Co ions (Table 2). Therefore, the role of Co ions played in photocurrent conversion processes is enhancing the separation of photogenerated electron–hole pairs and prolonging the lifetime of the charge carriers. Photocurrent onset potential of Co-STTF-2 moves toward the negative direction, which is more evidence supporting the decrease in surface recombination.[44]

CONCLUSIONS

Ti ions were introduced into micro-nanostructured hematite films via an in situ solid-state reaction method. The amount of Ti ions could be increased from a low doping level of 2.2% with a hydrothermal method in previous work to values as large as ca. 19.7% in the present work, with the retention of the micro-nanostructure of the hematite films. The increased doping level enhanced the electrical conductivity, facilitated the separation and transport of electrons and holes, and led to the improvement of the photocurrent density. Adsorption of Co ions enhanced electron–hole separation, which further improved the photocurrent density. This in situ solid-state reaction method has potential applications for producing highly efficient photoactive materials by doping other materials or ions with a sufficient amount.

■ ASSOCIATED CONTENT

Supporting Information

Five additional figures and three tables elaborate on experimental results. This material is available free of charge via the Internet at http://pubs.acs.org.

■ AUTHOR INFORMATION

Corresponding Author

*E-mail: chye@issp.ac.cn.

Notes

The authors declare no competing financial interest.

■ ACKNOWLEDGMENTS

This work was supported by National Basic Research Program of China (973 Program, Grant No. 2011CB302103), National Natural Science Foundation of China (Grant Nos. 11074255 and 11274308), and the Hundred Talent Program of the Chinese Academy of Sciences. We also appreciate SSRF for help in XANES experiments.

■ REFERENCES

(1) Miao, C. H.; Ji, S. L.; Xu, G. P.; Liu, G. D.; Zhang, L. D.; Ye, C. H. *ACS Appl. Mater. Interfaces* **2012**, *4*, 4428−4433.

(2) Brillet, J.; Grätzel, M.; Sivula, K. *Nano Lett.* **2010**, *10*, 4155−4160.

(3) Beermann, N.; Vayssieres, L.; Lindquist, S. E.; Hagfeldt, A. *J. Electrochem. Soc.* **2000**, *147*, 2456−2461.

(4) Wang, H.; Deutsch, T.; Turner, J. A. *J. Electrochem. Soc.* **2008**, *155*, F91−F96.

(5) Hahn, N. T.; Mullins, C. B. *Chem. Mater.* **2010**, *22*, 6474−6482.

(6) Meng, X. Y.; Qin, G. W.; Li, S.; Wen, X. H.; Ren, Y. P.; Pei, W. L.; Zuo, L. *Appl. Phys. Lett.* **2011**, *98*, 112104.

(7) Vayssieres, L.; Rabenberg, L.; Manthiram, A. *Nano Lett.* **2002**, *2*, 1393−1395.

(8) Robles-Águila, M. J.; Elizalde-González, M. P.; Mendoza, M. E.; Silva-Gonzáleza, R.; Yee-Madeira, H. *Surf. Interface Anal.* **2012**, *44*, 484−490.

(9) Cristobala, A. A.; Ramosb, C. P.; Bercoffc, P. G.; Bottaa, P. M.; Porto Lopeza, J. M. *Mater. Chem. Phys.* **2012**, *133*, 971−976.

(10) Guo, W. Q.; Malus, S.; Ryan, D. H.; Altounian, Z. *J. Phys.: Condens. Matter* **1999**, *11*, 6337−6346.

(11) Senderov, E.; Dogan, A.; Navrotsky, A. *Am. Mineral.* **1993**, *78*, 565−573.

(12) Pentcheva, R.; Nabi, H. S. *Phys. Rev. B* **2008**, *77*, 172405.

(13) Shen, S. H.; Jiang, J. G.; Guo, P. H.; Kronawitter, C. X.; Mao, S. S.; Guo, L. J. *Nano Energy* **2012**, *1*, 732−741.

(14) Fang, X. S.; Wu, L. M.; Hu, L. F. *Adv. Mater.* **2011**, *23*, 585−598.

(15) Droubay, T.; Rosso, K. M.; Heald, S. M.; McCready, D. E.; Wang, C. M.; Chambers, S. A. *Phys. Rev. B* **2007**, *75*, 104412.

(16) Lian, X. J.; Yang, X.; Liu, S. J.; Xu, Y.; Jiang, C. P.; Chen, J. W.; Wang, R. L. *Appl. Surf. Sci.* **2012**, *258*, 2307−2311.

(17) Tang, H. W.; Matin, M. A.; Wang, H. L.; Deutsch, T.; Al-Jassim, M.; Turner, J.; Yan, Y. F. *J. Appl. Phys.* **2011**, *110*, 123511.

(18) Kay, A.; Cesar, I.; Grätzel, M. *J. Am. Chem. Soc.* **2006**, *128*, 15714−15721.

(19) Barroso, M.; Cowan, A. J.; Pendlebury, S. R.; Grätzel, M.; Klug, D. R.; Durrant, J. R. *J. Am. Chem. Soc.* **2011**, *133*, 14868−14871.

(20) Liou, F. T.; Yang, C. Y. *J. Electrochem. Soc.* **1982**, *129*, 342−345.

(21) Wang, Y. M.; Yu, T.; Chen, X. Y.; Zhang, H. T.; Ouyang, S. X.; Li, Z. S.; Ye, J. H.; Zou, Z. G. *J. Phys. D: Appl. Phys.* **2007**, *40*, 3925−3930.

(22) McDonald, K. J.; Choi, K. S. *Chem. Mater.* **2011**, *23*, 4863−4869.

(23) Barroso, M.; Mesa, C. A.; Pendlebury, S. R.; Cowan, A. J.; Hisatomi, T.; Sivulab, K.; Grätzel, M.; Klug, D. R.; Durrant, J. R. *Proc. Natl. Acad. Sci. U.S.A.* **2012**, *109*, 15640−15645.

(24) Zhong, D. K.; Gamelin, D. R. *J. Am. Chem. Soc.* **2010**, *132*, 4202−4207.

(25) Peter, L. M.; Wijayantha, K. G. U.; Tahir, A. A. *Faraday Discuss.* **2012**, *155*, 309−322.

(26) Duval, Y.; Mielczarski, J. A.; Pokrovsky, O. S.; Mielczarski, E.; Ehrhardt, J. J. *J. Phys. Chem. B* **2002**, *106*, 2937−2945.

(27) Ensling, D.; Stjerndahl, M.; Nytén, A.; Gustafsson, T.; Thomas, J. O. *J. Mater. Chem.* **2009**, *19*, 82−88.

(28) Edstrom, K.; Gustafsson, T.; Thomas, J. O. *Electrochim. Acta* **2004**, *50*, 397−403.

(29) http://srdata.nist.gov/xps/Default.aspx. Accessed August 2012.

(30) Zhang, P.; Kleiman-Shwarsctein, A.; Hu, Y. S.; Lefton, J.; Sharma, S.; Forman, A. J.; McFarland, E. *Energy Environ. Sci.* **2011**, *4*, 1020−1024.

(31) Saremi-Yarahmadi, S.; Wijayantha, K. G. U.; Tahir, A. A.; Vaidhyanathan, B. *J. Phys. Chem. C* **2009**, *113*, 4768−4778.

(32) Reddy, B. M.; Chowdhury, B.; Smirniotis, P. G. *Appl. Catal., A* **2011**, *211*, 19−30.

(33) Armelao, L.; Bertoncello, R.; Crociani, L.; Depaoli, G.; Granozzi, G.; Tondello, E.; Bettinelli, M. *J. Mater. Chem.* **1995**, *5*, 79−83.

(34) Zeng, S. Y.; Tang, K. B.; Li, T. W. *J. Colloid Interface Sci.* **2007**, *312*, 513−521.

(35) Ankudinov, A. L.; Nesvizhskii, A. I.; Rehr, J. J. *Phys. Rev. B* **2003**, *67*, 115120.

(36) Fujikawa, T.; Matsuura, T.; Kuroda, H. *J. Phys. Soc. Jpn.* **1983**, *52*, 905−912.

(37) Magnan, H.; Stanescu, D.; Rioult, M.; Fonda, E.; Barbier, A. *Appl. Phys. Lett.* **2012**, *101*, 133908.

(38) Xu, G. P.; Ji, S. L.; Miao, C. H.; Liu, G. D.; Ye, C. H. *J. Mater. Chem.* **2012**, *22*, 4890−4896.

(39) Shaukatali, N. I.; Ingole, P. P.; Santosh, K. H. *ChemPhysChem* **2008**, *9*, 2574−2579.

(40) Ang, C.; Yu, Z.; Cross, L. E. *Phys. Rev. B* **2000**, *62*, 228−236.

(41) Arnold, M. S.; Avouris, P.; Pan, Z. W.; Wang, Z. L. *J. Phys. Chem. B* **2003**, *107*, 659−663.

(42) Karppinen, M.; Fjellvåg, H.; Konno, T.; Morita, Y.; Motohashi, T.; Yamauchi, H. *Chem. Mater.* **2004**, *16*, 2790−2793.

(43) Klahr, B.; Gimenez, S.; Fabregat-Santiago, F.; Hamann, T.; Bisquert, J. *J. Am. Chem. Soc.* **2012**, *134*, 4294−4302.

(44) Wijayantha, K. G. U.; Saremi-Yarahmadi, S.; Peter, L. M. *Phys. Chem. Chem. Phys.* **2011**, *13*, 5264−5270.